

A Methodology for Investigating New Nonprecious Metal Catalysts for PEM Fuel Cells

D. Susac,[†] A. Sode,[†] L. Zhu,[†] P. C. Wong,[†] M. Teo,[†] D. Bizzotto,[†] K. A. R. Mitchell,[†]
R. R. Parsons,[‡] and S. A. Campbell^{*,§}

Department of Chemistry, University of British Columbia, 2036 Main Mall, Vancouver, British Columbia, Canada V6T 1Z1, Department of Physics and Astronomy, University of British Columbia, 6224 Agricultural Road, Vancouver, British Columbia, Canada V6T 1Z1, and Ballard Power Systems Inc., 9000 Glenlyon Parkway, Burnaby, British Columbia, Canada V5J 5J8

Received: December 22, 2005; In Final Form: April 7, 2006

This paper reports an approach to investigate metal–chalcogen materials as catalysts for the oxygen reduction reaction (ORR) in proton exchange membrane (PEM) fuel cells. The methodology is illustrated with reference to Co–Se thin films prepared by magnetron sputtering onto a glassy-carbon substrate. Scanning Auger microscopy (SAM), X-ray photoelectron spectroscopy (XPS), energy-dispersive X-ray spectroscopy (EDX), and X-ray diffraction (XRD) have been used, in parallel with electrochemical activity and stability measurements, to assess how the electrochemical performance relates to chemical composition. It is shown that Co–Se thin films with varying Se are active for oxygen reduction, although the open circuit potential (OCP) is lower than for Pt. A kinetically controlled process is observed in the potential range 0.5–0.7 V (vs reversible hydrogen electrode) for the thin-film catalysts studied. An initial exposure of the thin-film samples to an acid environment served as a pretreatment, which modified surface composition prior to activity measurements with the rotating disk electrode (RDE) method. Based on the SAM characterization before and after electrochemical tests, all surfaces demonstrating activity are dominated by chalcogen. XRD shows that the thin films have nanocrystalline character that is based on a Co_{1-x}Se phase. Parallel studies on Co–Se powder supported on XC72R carbon show comparable OCP, Tafel region, and structural phase as for the thin-film model catalysts. A comparison for ORR activity has also been made between this Co–Se powder and a commercial Pt catalyst.

1. Introduction

The commercialization of electric vehicles for the 21st century depends on the development of less expensive power sources. At present, the hydrogen air-powered proton exchange membrane (PEM) fuel cells are favored for use in automobiles, due to their high-energy efficiency, low operating temperature ($\sim 80^\circ\text{C}$), and environmentally friendly character.^{1,2} Currently, these devices use Pt for both cathode and anode, with poly(perfluorosulfonic) acid as the proton-transfer electrolyte. Although recent technological improvements have reduced the amount of Pt required ($< 1\text{ mg cm}^{-2}$) by optimizing the particle size and catalyst dispersion,^{2,3} the market-price limitations for mass production have not yet been satisfied.

The performance of current PEM fuel cells is limited by a high overpotential and slow kinetics for the oxygen reduction reaction (ORR) at the cathode. A significant body of research exists on the characterization and modification of the nature of Pt catalysts (e.g., by alloying with Co, Fe, Cu, Cr) for increased activity^{4–8} and on the mechanism of ORR.^{9–11} Less has been done to date on the search for non-Pt catalysts, which are expected to be cheaper than Pt. To be effective, such catalysts must remain stable in the acidic environment of PEM fuel cells, and ideally, they should approach Pt's level of activity for ORR.

The pursuit of nonprecious metal catalysts for use in PEM fuel cells has been largely the purview of fundamental academic research, for example based upon biological catalyst systems for O_2 reduction. In this context, a number of groups studied complex porphyrins, including their heat treatments for enhanced catalytic activity.^{12–17} One direction has emphasized Co and Fe macrocycles, but these materials are expensive, and there exist uncertainties due to the pyrolysis that is necessary for ORR activity.¹⁸ Transition metal carbo–nitrides provide promising alternatives,^{19,20} but they also require heat treatments with a consequent increase in the energy expenditure. Metallic oxides (e.g. spinels, perovskites, and pyrochlores) that are active in alkaline fuel cells are generally insufficiently stable in acid, but the ORR performance most comparable to Pt has been obtained from transition metal chalcogenide phases based on Mo, Ru, and Se, which may also include C and O.^{21–28}

A common approach to searching out new catalysts has been to determine the activity of a dispersed catalyst onto a support material like carbon, but the comparisons generally suffer from incomplete information such as the active surface area, the composition and structure of the catalyst, and long-term stability. To illustrate an important challenge, it is noted that CO stripping voltammetry provides a well-established approach for determining the active surface area of Pt catalysts,^{29–31} but this approach is not generally applicable for other materials. Therefore, when various different catalysts are prepared in supported form, a direct comparison of their performance with a standard Pt catalyst is limited by their unknown active surface area.

* To whom correspondence should be addressed. E-mail: stephen.campbell@ballard.com.

[†] Department of Chemistry, University of British Columbia.

[‡] Department of Physics and Astronomy, University of British Columbia.

[§] Ballard Power Systems, Inc.

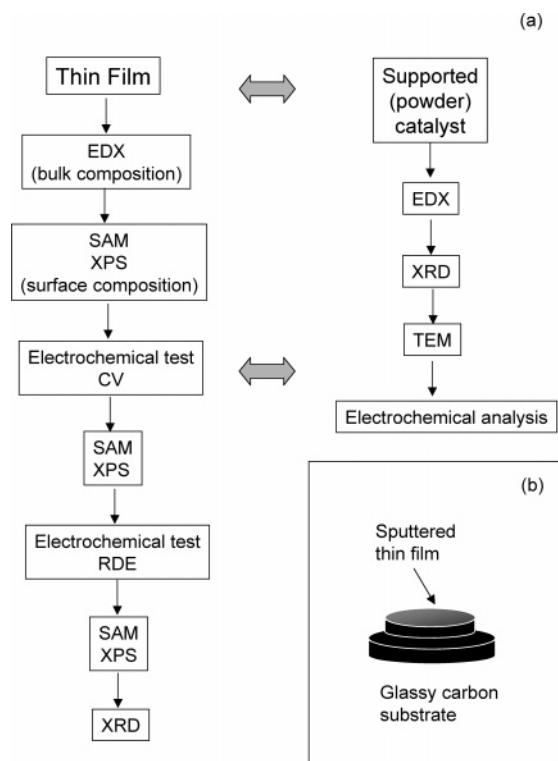


Figure 1. (a) Schematic representation of the methodological approach. (b) Shape of glassy carbon substrate.

This paper describes work that is part of a wider program that aims to overcome these challenges and to investigate ORR catalysts based on nonprecious metals in combination with chalcogens. The philosophy followed is illustrated here with reference to catalysts formed from Co and Se and prepared as thin films by sputter deposition on glassy-carbon substrates. The idea of using Co chalcogenides is not new,³² but there has been little systematic study under well-controlled conditions. A comparable thin-film approach was used previously to characterize Co carbo-nitrides as ORR catalysts.³³

Figure 1a illustrates the approach taken in our work. The nature of the films formed are evaluated by a range of characterization methods. Specifically, energy-dispersive X-ray spectroscopy (EDX) and X-ray diffraction (XRD) are used to characterize the bulk materials, and scanning electron microscopy (SEM), scanning Auger microscopy (SAM), and X-ray photoelectron spectroscopy (XPS) are used to characterize the surfaces. Electrochemical measurements are made by cyclic voltammetry under both stationary and dynamic conditions, and the surface characterizations of the films are performed before and after the electrochemical treatments to identify any topographical and compositional changes occurring.

The methodology introduced aims to compare the catalysts prepared in thin-film form with comparable materials dispersed on high-area carbon supports. The motivation for studying model thin-film samples is to gain enhanced insight into the chemical compositions and structures required to develop new dispersed catalysts for the ORR. This paper reviews progress toward this objective and discusses the new knowledge gained to date for the Co–Se system.

2. Experimental Section

2.1. Thin Film Preparation. The substrates for the thin film deposition were machined from a glassy-carbon plate (Tokai Carbon) in a “top hat” shape (Figure 1b) with a working surface

area of 1.23 cm². Individual samples were first polished with SiC paper (P4000 Microcut, Buehler), and they were subsequently polished with 6 and 1 μm diamond suspension (Leco) sprayed onto a polishing microcloth (Buehler). The substrates were ultrasonically rinsed for 2 min in deionized water between each polishing stage and for 2 min in acetone (HPLC grade, Fisher Scientific) after the final polishing step.

Thin films containing Co and Se were prepared in a sputter coater system (model V3T, Corona Vacuum Coaters Inc.), which was modified for dual deposition. Two planar magnetron sputter sources (Corona Vacuum Coaters Inc.), each 5 cm in diameter, were oriented for simultaneous deposition onto the glassy-carbon substrate with the target-to-substrate distance set at 11 cm. The magnetrons could be operated in either direct current (dc) or radio frequency (rf) (13.6 MHz) modes. The former was used for the Co target, and rf power was used for the Se and Co–Se composite targets (described below). Prior to film deposition, the system was turbomolecular pumped to a base pressure of 3×10^{-6} Torr (4×10^{-4} Pa). The plasma discharge was operated at a pressure of 3.5×10^{-3} Torr (4.7×10^{-1} Pa) with a continuous, throttled flow of argon (99.9%), and the targets were presputtered for at least 10 min prior to moving the substrate into the deposition zone. A bias of –180 V was applied to the substrate for the first minute of deposition; the objective was to allow some early ion bombardment to help promote the subsequent film adhesion. A –75 V bias was applied for the remaining deposition.

The initial sputtering was performed using the separate elemental targets of Co (99.95% purity, Kurt Lesker) and Se (99.99% purity, Angstrom Sciences). Because it was hard to avoid sublimation during sputtering of the Se target (resulting from its low thermal conductivity and low melting point), Co–Se composite targets were used, fabricated by mixing together equal weights of Co (~100 mesh, 99.9% purity, Aldrich) and Se (pellets ~2 mm dimension, 99.999% purity, Aldrich) and then melting in a mold (5-cm diameter). The presence of Co grains increased the thermal conductivity, thereby allowing the composite target to be sputtered with significantly reduced Se sublimation. The film compositions were controlled by varying the powers to the targets, and initial test samples were investigated to determine the sputtering conditions to achieve films of 0.4–0.5 μm thickness. Film thickness measurements were made with a Tencor Alfa Step profilometer. For each set of sputtering conditions, a number of films were prepared. The bulk compositions of these films were consistent to within 5 at. %.

2.2. Composition and Structure Characterization of Thin Films. EDX spectroscopy was used to determine bulk elemental compositions of the thin films. The spectra were measured with a Hitachi S2300 spectrometer (20 keV incident electron beam), and the elemental peaks were converted to atomic percentages following standard procedures³⁴ using Xone software. Surface topography images were measured by SEM and surface compositions were measured by SAM; both analyses were made using a Microlab 350 spectrometer (Thermo Electron Corp.) that was equipped with a field emission source and a hemispherical energy analyzer. In SAM, the electron beam can be either rastered across a selected area (e.g., side 10 μm), for average surface composition, or, in spot analysis mode, the beam is directed to a particular region of interest (smallest dimension ≈ 15 nm). Both Auger analyses were performed on different surface regions, with the primary electron beam set at 10 keV and 3.5 nA, and the analyzer operated in the constant retardation ratio mode. Elemental amounts were estimated by SAM from

peak areas,³⁵ using sensitivity factors provided by the manufacturer. A depth profile was measured using the Ar⁺ ion beam operated at 3 kV and 1 μAcm^{-2} ion density.

XPS spectra were measured with a Leybold MAX200 spectrometer using a Mg K α source (1253.6 eV) operating at 15 kV and 20 mA, with the pass energy set at 48 eV. Binding energies were referenced to the Au 4f_{7/2} peak at 84.0 eV for conducting samples, but for the Se standard that exhibited charging, the C 1s peak from adventitious hydrocarbon contamination was set at 285.0 eV as the alternative reference. To obtain a spectrum from clean Co metal, a thin Co film was deposited onto glassy carbon and then sputtered (20 min Ar⁺ bombardment, ion energy 1.5 kV) in the XPS chamber to remove adsorbed C and O. Characterizations by XRD were performed in a Bruker D8 advanced diffractometer with Cu K α radiation source ($\lambda = 1.5418 \text{ \AA}$). Intensities were recorded as the scattering angle, 2θ , varied from 5 to 90° at 0.02° s⁻¹.

2.3. Electrochemical Characterization. The catalytic activity of the Co–Se thin films was studied by cyclic voltammetry in O₂-saturated 0.1 M H₂SO₄ using an Eco-Chimie PG30 (Autolab) potentiostat. Electrochemical measurements without rotation (denoted as CV hereafter in the text) used a standard three-electrode glass cell with a saturated calomel electrode (SCE) as the reference (connected by a salt bridge) and a Pt wire as the counter electrode. For consistency, all potentials quoted after CV have been converted to the scale with respect to the reversible hydrogen electrode (RHE). The potential on the stationary thin-film working electrode was scanned with sweep rates ranging from 100 to 1100 mV s⁻¹. For the dynamic polarization measurements (denoted as RDE), each thin film was used as a rotating disk electrode with the rotator (AFMSRX, Pine Instruments) in a three-compartment electrochemical cell; a reversible hydrogen electrode (RHE) connected to the Luggin capillary acted as the reference, and a Pt gauze acted as the counter electrode. In these experiments, the rotation speeds varied from 500 to 2000 rpm. The onset acquisition potential for obtaining the polarization curves was set 50 mV positive to the open circuit potential (OCP). This aided the determination of experimental crossover potential (equilibrium potential). The RDE holder was specially designed to accommodate the top-hat-shaped glassy-carbon substrate, which allowed transfer between the electrochemical and surface science characterization systems. The polished glassy-carbon surface, onto which the Co–Se thin film was deposited, was leveled with the holder to prevent any hydrodynamic artifacts during the electrode rotation.

Solution cleanliness was regularly assessed by measuring the voltammogram for a Pt RDE (diameter 3 mm, Ω Metrohm) and checking that it closely matched literature reports.^{34,35} The ORR reaction on the analytical Pt RDE electrode gave a Tafel slope of -120 mV dec^{-1} in a potential range 0.5–0.7 V (vs RHE), in agreement with published data.^{9,37} The catalytic activity of each Co–Se thin film was evaluated against the performance of an electrode formed by a thin film of Pt sputtered onto the glassy-carbon substrate. This ensured the same area as the Co–Se samples and indicated an advantage of the thin-film approach. The purity of the Pt thin film was confirmed by EDX and SAM measurements, and its electrochemical response was consistent with that from the analytical Pt electrode.

2.4. Supported Powder Catalyst Preparation and Characterization. The powder catalyst was made using a 50 wt % Co loading on XC72R carbon (Cabot), and the nominal Co/Se ratio was 2:1. Carbon (1 g) was dispersed in a beaker with 1 dm³ of water (type 1, 18 M Ωcm) using magnetic stirring, and a few mL of propan-2-ol (Fisher Scientific) was added to aid

TABLE 1: Elemental Compositions from EDX (Atomic %) for the Three As-Prepared Co–Se Thin Films Discussed in the Text

	Co	Se	Se/Co
TF1	72.5	27.5	0.4
TF2	51.6	48.4	1.0
TF3	43.5	56.5	1.3

wetting. Sufficient amounts of Co (as CoCl₂·6H₂O, Aldrich) and Se (as SeO₂, Aldrich) were added, and the mixture was stirred for 1 h before introducing 500 mL of 0.2 M NaBH₄ at a rate of approximately 1 drop s⁻¹. Following the complete addition of NaBH₄, the mixture was stirred for an additional 1 h, after which the powder was filtered, washed twice with type-1 water, and dried. The dry powder was placed in a porcelain combustion boat, introduced into a tube furnace, and heated in a N₂ atmosphere to 600 °C for 4 h. At completion, it was noticed that red deposits of Se had formed on the cooler parts of the furnace tube, indicating that the Se content in the powder was less than the amount introduced into the preparation.

Ex situ powder characterization was undertaken using transmission electron microscopy (TEM) (Hitachi H-800 with a Quartz XONE EDX, operated in STEM mode at 100 keV electron beam energy), EDX, and XRD analysis (Section 2.2). For the TEM analysis, a small portion of the powder catalyst was dispersed in 1 mL of ethanol and then micropipetted onto a thin Cu grid substrate specifically designed to trap small particles.

The electrochemical activity and stability of the supported catalyst was evaluated by RDE measurements at 2000 rpm (Pine Instruments rotator AFMSRX) in O₂-saturated 0.5 M H₂SO₄ solution at 30 °C, using a conventional three-electrode cell with separate compartments for the counter (Pt wire) and reference (RHE) electrodes. The working electrode was formed by depositing catalyst onto the surface of a glassy-carbon electrode (5-mm diameter, Pine Instruments AFMI 1980GCHT), which had first been polished with 0.05 μm Al₂O₃. The deposition used the following procedure: 20 mg of powder was ultrasonically dispersed in 2 mL of glacial ethanoic acid, and 5 μL of that dispersion was then pipetted onto the electrode surface and dried in hot air. It was found that the addition of Nafion solution was not necessary to prevent a loss of the catalyst from the disk over the time frame of the experiments. The RDE measurements were made by recording the current as the potential was swept from the OCP to 0.1 V vs RHE at 5 mV s⁻¹ (PAR 263A potentiostat).

For the comparison of activity, electrochemical measurements were repeated using: 40 wt % of Pt on XC72R (Johnson Matthey HiSpec 4000), the equivalent amount of XC72R with no catalyst, a blank glassy-carbon disk, 50 wt % of Co on XC72R, and 15 wt % Se on XC72R.

3. Results and Discussion

Table 1 reports chemical compositions obtained from EDX analysis for the three as-prepared thin films discussed in this paper. These surfaces, to be assessed as model catalysts, were prepared as noted in Section 2.1 by sputter deposition onto the glassy-carbon substrates. The samples designated TF1 and TF3 were deposited by using both the Co target and the composite Co–Se target, whereas TF2 was formed by sputtering the individual elemental targets. The probe depth for EDX ($\geq 1 \mu\text{m}$) gives bulk composition, according to which the sample designated TF1 is Co-rich, whereas TF2 and TF3 have elemental ratios closer to stoichiometric CoSe. SEM micrographs shown in Figure 2a–c indicate that the as-prepared samples have

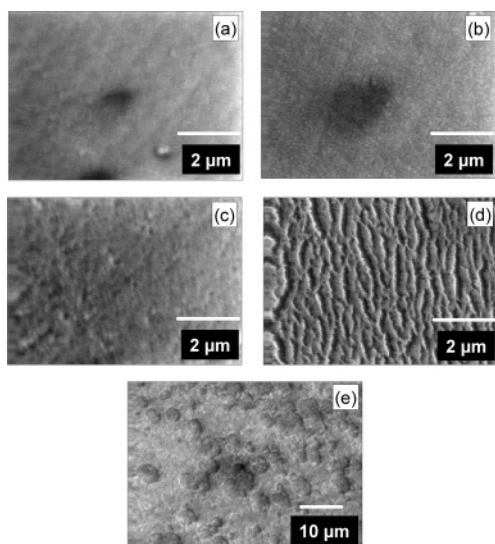


Figure 2. SEM micrographs of sputtered Co–Se thin films: (a) TF1, (b) TF2, (c) TF3, (d) TF1 after CV, and (e) TF1 after RDE.

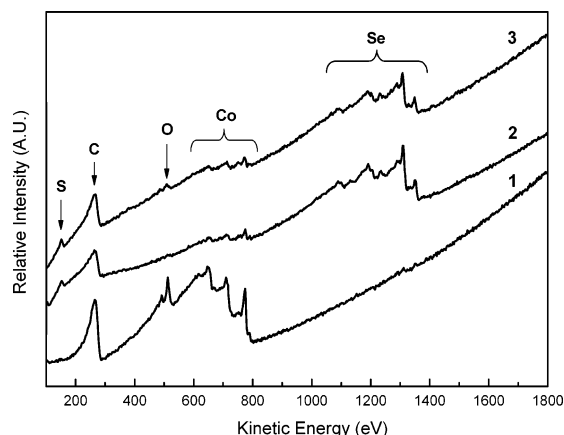


Figure 3. Auger spectra measured from TF1: (1) as prepared, (2) after CV, and (3) after RDE.

TABLE 2: Elemental Composition (Atomic %) from SAM for TF1 in the As-Prepared State and After the Two Electrochemical Analyses

	Co	Se	C	O	S	Se/Co
as prepared	5.1	2.6	89.0	3.3	<i>a</i>	0.5
after CV	1.4	19.4	74.1	<i>a</i>	5.1	13.7
after RDE	1.9	13.8	69.8	1.4	13.1	7.2

^a Not detected.

smooth surfaces; multiple SAM measurements were taken from different regions to confirm that each sample was chemically homogeneous. The probe depth for SAM (≤ 10 nm) is much less than for EDX, and therefore, SAM emphasizes composition in the near-surface regions.

3.1. Surface and Electrochemical Characterization of TF1.

Figure 3 shows microarea Auger spectra measured from TF1 in the “as prepared” state as well as after the CV and RDE electrochemical treatments. The Co LMM transitions occur in the 620–800 eV kinetic energy range, whereas the Se LMM transitions occur from 1160 to 1360 eV. Besides these elements, a small amount of O is identified at 513 eV in spectrum 1, and all three spectra show C signals at 267 eV due to air exposure and handling. Table 2 provides Auger elemental quantification information based on measurements taken from different regions on the sample. The surface composition of TF1 is chemically homogeneous across the sample and, besides the air-borne C,

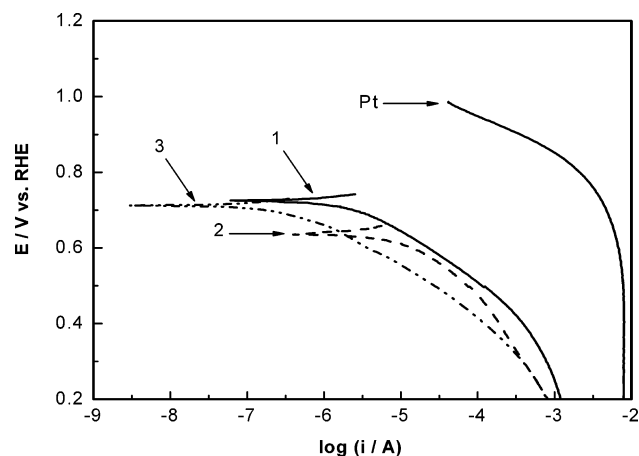


Figure 4. Polarization curves measured for the thin films: (1) TF1, (2) TF2, (3) TF3, and compared with that of Pt; all measurements done in O_2 -saturated 0.1 M H_2SO_4 at 25 °C, using 2000 rpm rotation speed.

is dominated by Co. No Ar^+ sputtering was applied to remove the air-borne C; this was deliberate to avoid any change in the chemical state prior to the electrochemical characterizations. However, with test thin-film samples prepared under similar conditions, it was confirmed that the C and O are both removed by 2 min of Ar^+ bombardment, and that the chemical compositions are homogeneous in depth. The surface Se/Co ratio shows a $\sim 25\%$ increase compared with the bulk value obtained from EDX; in part, at least, this appears as a consequence of the use of magnetron sputtering for sample fabrication, where there can be variations in elemental sublimation and adsorption at the end of the process as the sample cools (typically from around 60–80 °C).

Following the EDX and SAM characterizations, the TF1 film was electrochemically characterized. CV was performed under stationary electrode conditions in O_2 -saturated 0.1 M H_2SO_4 to measure the open circuit potential (OCP) and to observe the O_2 reduction. Initially, a low OCP value of 0.06 V vs RHE was measured from TF1, which was consistent with its Co-rich surface. Nevertheless, for immersions of 15 min and longer, the OCP increased to 0.60 V vs RHE and remained stable. This was an indication of a change in the surface chemical composition.

After the first electrochemical test, TF1 was taken out of the holder and reanalyzed using SAM. The SEM micrograph (Figure 2d) shows that, in contrast to the smooth surface of the as-prepared form, the CV process has created a network of narrow microchannels, which indicated dissolution. The Auger analysis (Figure 3, spectrum 2) confirmed a significant change in chemical composition. The original Co-dominated surface was transformed into one that is highly Se rich (Se/Co ratio = 13.7). This change in the TF1 film surface parallels the change in OCP. The preferential Co dissolution is found to be even more pronounced within the narrow channels where the Se/Co ratio increases to as much as 19.0. Furthermore, although no O was found at the TF1 surface after CV, some S and C was detected (Table 2), the latter expected from the air exposure.

The second electrochemical test utilized TF1 as a rotating disk electrode. The electrochemical polarization curves for various electrode rotation speeds have been determined based on measured ORR reduction curves in fresh O_2 -saturated H_2SO_4 electrolyte. Figure 4, curve 1 shows the polarization curve obtained at room temperature with rotation at 2000 rpm. It is shown that TF1 exhibits catalytic activity for ORR, although the kinetic current is several orders of magnitude smaller than

TABLE 3: Elemental Ratios from Auger Electron Spectroscopy for the Three Co–Se Thin Films after the Two Electrochemical Analyses Discussed in the Text

thin film	after CV			after RDE		
	Se/Co	S/Se	(S+Se)/Co	Se/Co	S/Se	(S+Se)/Co
TF1	13.7	0.3	17.4	7.2	1.0	14.0
TF2	5.0	0.3	6.7	5.3	0.8	9.2
TF3	13.7	0.4	18.7	11.3	0.3	15.1

that for the Pt thin-film electrode. The equilibrium potential is 0.74 V vs RHE, and the linear Tafel region (0.5–0.7 V vs RHE) gives a Tafel slope of -133 mV dec^{-1} .

The morphology and surface composition of TF1 was examined after the RDE test. The micrograph (Figure 2e) indicated that the TF1 surface had suffered further dissolution, but the underlying glassy-carbon substrate was not exposed. Auger analysis from different areas across the sample showed that this new surface is laterally homogeneous with regard to elemental composition and is still Se-rich (Figure 3, spectrum 3). The Se/Co ratio decreased to 7.2 after the RDE test, suggesting that some Se dissolution may have occurred as well (Table 2). Only a small amount of O was measured, but the S content increased. The S/Se ratio of 0.3 after CV grew to 1.0 after RDE, thereby indicating a likely exchange between Se and S. The total chalcogen-to-metal ratio (given as (S + Se)/Co in Table 3) decreased from 17.4 to 14.0.

The origin of the S has not yet been unambiguously established, but our current understanding is that side reactions occur in the sulfuric acid electrolyte that may result in some Se being replaced by S.³⁸ Further studies are planned to clarify this issue. The data obtained from this compositional analysis of TF1 clearly justify the importance of using the surface sensitive techniques such as SAM to examine the film surface, especially after electrochemical measurements. Without knowing the surface chemical composition of the thin films after examination for ORR activity, their catalytic performance could be mistakenly assigned to the as-prepared film surface.

3.2. Nature of TF1. Evidence in Section 3.1 showed that the thin Co–Se film designated TF1 is active for ORR and that the surface composition responsible for such activity is significantly different from the as-prepared state. The CV process, in effect, acts as a pretreatment step, which allows leaching of soluble components (e.g., metallic Co) from the film surface prior to the RDE measurements in fresh electrolyte. The surface after CV, with the enhanced chalcogen-to-metal ratio, was active for ORR. In addition, according to Auger analysis after RDE, the sample's surface remains dominated by chalcogens, and the remaining Co in the surface region is believed to be bonded to chalcogen, thereby becoming stable in the acid environment.

The performance of the Se thin film for oxygen reduction was tested as well. Although its OCP was 0.70 V vs RHE, this film did not show any appreciable ORR activity, which was consistent with previous reports.^{39,40} This suggests that a species at the TF1 surface with Co–chalcogen bonding is responsible for the observed ORR activity. High-resolution Auger and XPS spectra were measured to obtain more information on the nature of the TF1 catalyst.

Figure 5a compares Co LMM Auger spectra measured from a high purity Co sample (spectrum 1) and from TF1 after RDE (spectrum 2). These spectra are dominated by the L_3VV , $L_3M_{23}V$, and $L_3M_{23}M_{23}$ transitions at around 773, 711, and 649 eV, respectively, on the kinetic energy scale. In comparison to pure Co, the Co LMM spectrum from TF1 after electrochemical

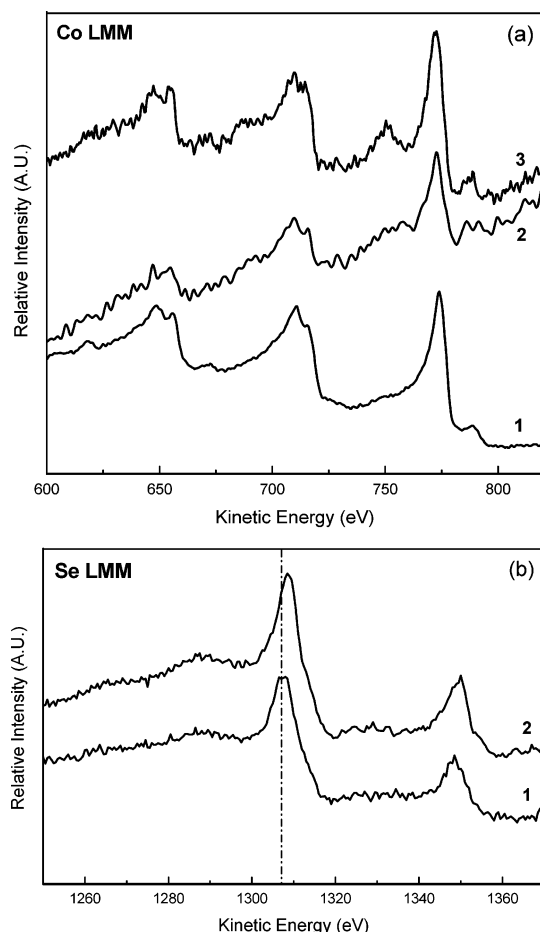


Figure 5. Auger spectra measured for: (a) Co LMM from (1) Co thin film, (2) TF1 after RDE, and (3) TF2 after RDE; (b) Se LMM from (1) Se standard and (2) TF1 after RDE.

characterization shows an enhanced transition in the vicinity of 750 eV, which is believed to be a signature of Co–chalcogen bonding.

More subtle changes are seen for the Se LMM spectra. Figure 5b compares the spectrum measured from the high-purity Se thin-film standard with that from TF1 after RDE (spectra 1 and 2, respectively). The spectral shapes are similar, but the main Se $L_3M_{45}M_{45}$ peak for the TF1 film shows a shift of 1.2 eV to higher kinetic energy as compared to the high-purity thin-film sample. The observed shift is likely a result of charge transfer from metal to chalcogen as a result of the Co–Se bonding. Comparable observations are also available from XPS. Figure 6a reports Se 3d spectra from the standard Se thin film (spectrum 1), whereas that from TF1 after RDE is shown as spectrum 2. The Se 3d peak measured from the Se standard occurs at 55.8 eV binding energy, which agrees with literature values.⁴¹ However, for TF1 after RDE, a 0.8 eV shift toward lower binding energy is observed for the Se 3d peak, which is consistent with the presence of Co–Se bonding. The Se 4s photoelectron peak provides further bonding information. Earlier work has shown that both Se 4s and S 3s appear as single peaks in transition metal monoselenides and monosulfides, whereas a doublet is characteristic for the diselenides and disulfides.⁴² Se 4s measured from TF1 after RDE shows a single peak at 14.2 eV, which ultimately supports the conclusion that the main chalcogenide phase present near the surface of TF1 is the Co-monoselenide rather than the diselenide, CoSe_2 . Additionally, the S 2p photoelectron peak occurs at 160.5 eV binding energy, which corresponds to S^{2-} ⁴¹ and therefore suggests a CoS-type

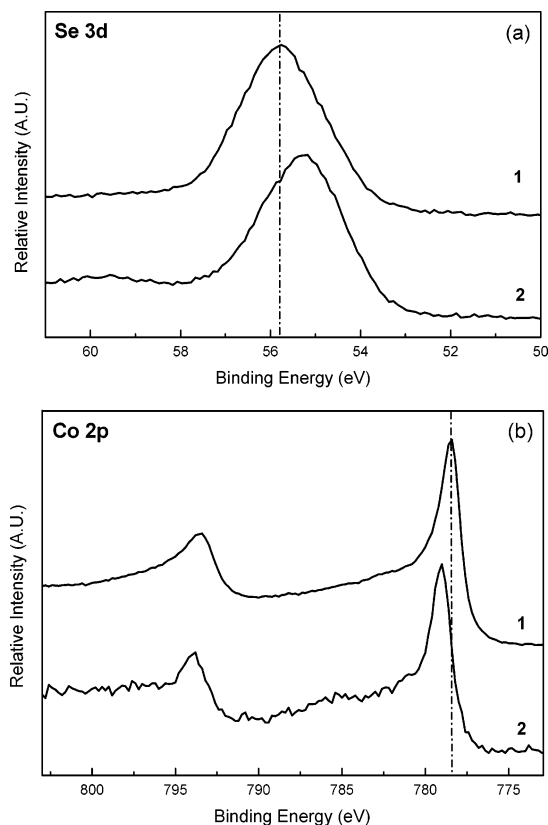


Figure 6. XPS spectra measured for: (a) Se 3d from (1) Se standard and (2) TF1 after RDE; (b) Co 2p from (1) Co standard and (2) TF1 after RDE.

structure. Figure 6b compares Co 2p photoelectron peaks measured from the Co standard (spectrum 1) and from TF1 after RDE (spectrum 2). The Co $2p_{3/2}$ peak from TF1 after electrochemical characterization is measured at 778.8 eV, which is shifted to higher binding energy by 0.3 eV compared to that measured for the Co standard. Low intensity shake-up satellites are also present in the TF1 spectrum between 782.0 and 790.0 eV; these observations are consistent with an earlier characterization of CoSe.⁴³

3.3. Comparison with TF2 and TF3. In contrast to Co-rich TF1, the bulk compositions of both TF2 and TF3 in their as-prepared forms are close to stoichiometric CoSe, with the Se/Co ratios equal to 0.9 and 1.2, respectively (Table 1). Despite having comparable bulk compositions, the surfaces of these thin films turned out to be different. Auger analysis indicated that Se is enriched at the TF2 surface, with the Se/Co ratio equal to 2.8, whereas the surface of TF3 was Co-rich and therefore more similar to that of TF1.

The first electrochemical treatment (CV) acted as a pretreatment step in which Co not bonded to Se dissolved from the surfaces of both TF2 and TF3. Interestingly, for TF2, the Se/Co ratio only doubled after CV, but TF3 behaved somewhat like TF1 insofar as its initially Co-rich surface transformed into one that is highly Se rich (Table 3). S was also detected in these films after CV. SEM micrographs for both TF2 and TF3 (not shown) showed no obvious change in film morphology after CV, in contrast to TF1.

Figure 4 shows polarization curves in O_2 -saturated electrolyte (RDE analysis). The equilibrium potential measured from TF2 (0.62 V vs RHE) is lower compared to TF1 and TF3, but no Tafel slope has been derived because of the narrow linear range. The Tafel region for TF3 is located in the same potential window as for TF1 (0.5–0.7 V vs RHE), with both samples showing

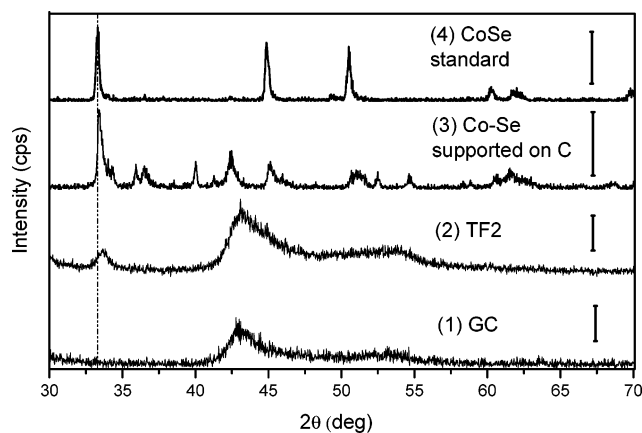


Figure 7. Diffractograms measured from: (1) glassy carbon, (2) TF2, (3) supported powder Co–Se catalyst, and (4) CoSe powder. In each case, the vertical bar corresponds to 100 counts s^{-1} .

similar Tafel slopes (-133 and -128 mV dec^{-1} for TF1 and TF3, respectively). The largest current in the kinetic region at, for example, 0.6 V vs RHE, is obtained for TF1. Following surface analysis after RDE, the composition of TF2 remains similar to that after CV, in terms of Se/Co ratio, but the S/Se ratio increases between the two electrochemical tests as in the case of TF1. Nevertheless, after RDE, the (S + Se)/Co ratio is lower compared with TF1 (Table 3). For TF3, the Se/Co ratio decreases slightly after RDE, the S/Se ratio remains constant, but (S + Se)/Co reaches the high value of 15.1. The surface region of TF3 changes somewhat like that seen for TF1; in both cases, the initially Co-rich surface became transformed by RDE into one that is chalcogen rich.

High-resolution SAM and XPS spectra, measured from TF2 and TF3 after RDE, showed similar features to those reported for TF1 as being indicative of Co–chalcogen bonding. For example, the Co LMM transitions for TF2 (Figure 5a, spectrum 3) show an even more pronounced structure near 750 eV, and a shoulder appears on the low kinetic energy side of Co $L_{23}M_{23}V$ between 675 and 700 eV. The kinetic energy shifts for Se $L_{3}M_{45}M_{45}$ compared to the elemental standard were 1.5 and 1.0 eV for TF2 and TF3, respectively. Among the three films, TF2 has the largest shift, which we take to indicate the highest level of interaction between Co and Se within the Auger probe depth. The Se 3d photoelectron peak for both films occurred at 54.7 eV, and as for TF1, a single Se 4s peak was consistent with a monoselenide species. The chemical state of S is also shown to be in the sulfide form after RDE, as previously found for TF1.

3.4. Structural Aspects. The phase diagram for the Co–Se system at below 400 °C shows various stable phases, such as Co_9Se_8 , $Co_{1-x}Se$, and $CoSe_2$, depending on the Se content.⁴⁴ The sputtering process deposits atoms, but because no additional heating is done in this study, the films formed may not have reached equilibrium prior to the electrochemical tests. Additionally, because Se sublimation occurred during the sputtering process (Section 2.1), the thin films are also expected to contain some selenium in molecular form.

The crystallinity of the samples after RDE analysis was examined by XRD. Figure 7 reports diffractograms from glassy carbon (curve 1), from TF2 (curve 2), and from commercial CoSe powder (Alfa Aesar) (curve 4). Commercial CoSe has peaks at 33.3° , 44.3° , and 50.1° on the 2θ (scattering angle) scale. TF2 does not show a peak near 50° , but there is a small peak at 33.5° and a shoulder at 44.6° . The broad peak at 43.0° is due to glassy carbon. The peak at 33.5° has a width of 1.5°

(fwhm), which indicates that the diffracting phase is nanocrystalline in nature.⁴⁵ The same component is present in the diffractograms measured from TF1 and TF3. The slight difference in peak positions between the thin films and the CoSe standard is believed to be significant and is the subject of ongoing work. Comparison with the XRD database indicates that the nanocrystalline phase in the thin films is based on a Co_{1-x}Se phase.^{46,47}

The surface science characterizations in Sections 3.1 and 3.3 established that the thin-film surfaces have a high chalcogen content after ORR. This chalcogen-rich layer improves film stability by preventing electrochemical oxidation. Combining this information with the crystallographic observations suggests that the active sites may comprise nanocrystals of Co_{1-x}Se surrounded by extra chalcogen (such structural arrangements are indicated in our ongoing work using transmission electron microscopy).

4. Supported Powder Catalyst

The Co–Se powder supported on XC72R carbon prepared according to the procedure described in Section 2.4 has the following bulk composition determined by EDX (at. %): Co 16.2, Se 5.6, C 64.1, O 13.8, and trace amounts of S and Cl (~ 0.1 at. % each). The approximately spherical particles of Co–Se catalysts with diameter in the range of 10–100 nm were observed in TEM analysis. Larger agglomerates were also found. The average atomic composition of those particles was Co 42.5 at. % and Se 57.5 at. %. In addition, needlelike particles (length 50–100 nm) containing only Co, C, and O were observed, and they are believed to be carbide species formed by excess Co. This was broadly consistent with conclusions from the powder XRD analysis, which showed that the principal component of the Co–Se supported catalyst also corresponds to a Co_{1-x}Se phase (Figure 7, diffractogram 3), with some contribution from a carbide phase (peaks in the $35\text{--}44^\circ$ and $52\text{--}60^\circ$ ranges). The link thereby established between the model catalysts and those prepared conventionally justifies the methodological approach taken in this project and allows the chemistries of these materials to be compared directly.

Figure 8a shows the electrochemical reduction of oxygen for the various materials tested. The background currents from a polished glassy carbon (curve 1) and high surface area XC72R carbon deposited onto the glassy carbon (curve 2) are measured as references, whereas the activities from Co and Se supported on XC72R (curves 3 and 4 respectively) are compared to those of two Co–Se supported catalysts (curves 5 and 6, where the second has a double loading). In contrast to the inert glassy carbon, the XC72R carbon without any catalyst shows activity for oxygen reduction, although at a very large overpotential. The ORR reduction currents slightly increase with the addition of either Co or Se on XC72R, but the Co-supported catalyst was found to be unstable due to Co dissolution. A deep-pink Co(II) color developed overnight in the ethanoic acid used to disperse the catalyst. In addition, the OCP of Co supported on XC72R upon cycling quickly raised from low negative values (a few mV) to zero and to 0.70 V vs RHE, where the final value is similar to that from the carbon support. When the Co–Se supported catalysts were dispersed in ethanoic acid overnight, a much paler pink color developed, thus suggesting that more Co became stabilized by bonding with Se. The Co–Se supported powder catalyst is the only one that shows a peaked response (Figure 8a, curves 5,6) similar to that reported for the catalyst based on cobalt carbo-nitride.⁴⁸ The activity from the Co–Se powder is a function of the quantity of catalyst used, because

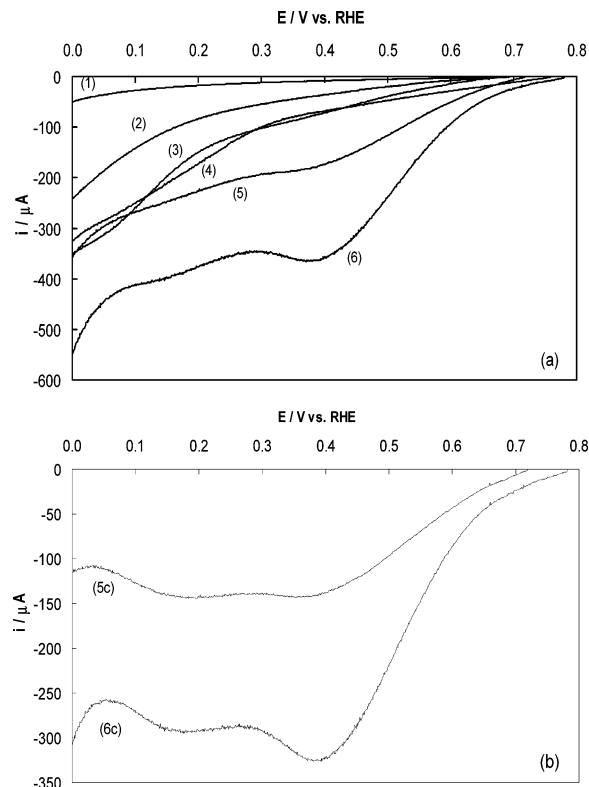


Figure 8. (a) ORR cathodic curves measured from: (1) polished glassy carbon, (2) XC72R carbon, (3) Co on XC72R, (4) Se on XC72R, (5) Co–Se on XC72R single loading, and (6) Co–Se on XC72R double loading; (b) curves (5) and (6) after background correction (subscript c); all measurements done in O_2 -saturated 0.5 M H_2SO_4 at 30°C , using 2000 rpm rotation speed.

the measured current approximately doubles with the doubling of the amount of catalyst (Figure 8a, curve 6). This suggests that the current is limited kinetically rather than by mass transport within the porous catalyst deposit.

Figure 8b shows the ORR response for the supported Co–Se catalyst (curve 5c for single loading and curve 6c for double loading) following a correction that involves subtracting the current from the XC72R carbon alone. Although simplistic, this approach should, in part at least, indicate the response of the Co–Se catalyst without the influence of the carbon support, thereby enabling comparison with the thin-film catalysts reported in Sections 3.1 and 3.3. After electrochemical analysis, a small amount of Co–Se supported powder was removed from the surface of the glassy-carbon electrode using ultrasonic rinsing. The TEM/EDX measurements indicated that the supported catalyst still contained the spherical-like Co–Se particles, but the carbide phase had dissolved. It is known that S is the major contaminant in Vulcan carbon.⁴⁹ From that perspective, it is difficult to investigate any S–Se exchange that might have happened during the electrochemical analysis of supported powder. This again illustrates the value of studying the model catalysts in thin-film form.

The dispersed and thin-film catalysts show similar behaviors, but with some differences in detail. Both types are active for ORR, although their activities cannot be directly compared because the surface area of the powder is not defined. The OCP for the powder (0.78 V vs RHE) is slightly higher than that for TF1 (0.74 V vs RHE), which has the highest value of the thin films studied. Thus far, no attempt has been made to optimize the behaviors of either type of catalyst, but their general relationship follows from similar Co–Se structural phases being present in the dispersed and thin-film forms.

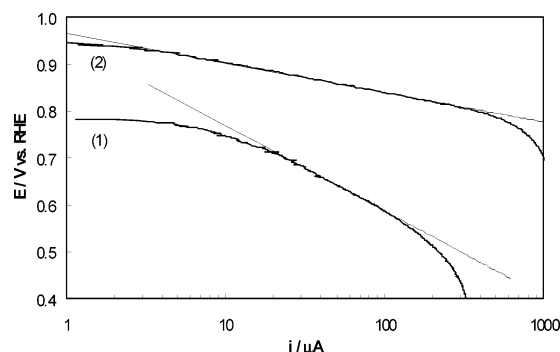


Figure 9. Tafel plots for: (1) Co–Se supported catalyst after background correction, and (2) commercial Pt supported catalyst (HiSpec4000); all measurements done in O_2 -saturated 0.5 M H_2SO_4 at 30 °C, using 2000 rpm rotation speed.

Another comparison is with platinum. The data from Figure 8b for curve 6_c is replotted to construct the Tafel plot shown in Figure 9, curve 1, where it is compared to a similar plot (Figure 9, curve 2) for a commercial platinum catalyst (Johnson Matthey HiSpec4000) at half the total metal loading. It appears that similar rates of reaction at similar overpotentials, measured from their respective equilibrium potentials, can be obtained for both catalysts, but the equilibrium potential for the noble metal catalyst is significantly higher. The Tafel slope for the dispersed Co–Se catalyst is -167 mV dec^{-1} , in the potential range 0.5–0.7 V (vs RHE). The high Tafel slope for the former compared to the value for Pt (-120 mV dec^{-1}) indicates the need for comparative mechanistic studies.

5. Concluding Remarks

This paper describes the methodology used to investigate nonprecious metal catalysts for the oxygen-reduction reaction in PEM fuel cells. Model thin-film Co–Se catalysts have been prepared by magnetron sputtering, and their activities for ORR were compared against a Pt standard. The approach, illustrated with reference to three Co–Se thin films that were prepared with different compositions, has two main advantages. First, direct comparisons can be made between different thin-film catalysts because they have similar surface areas. Second, surface analysis can be used to allow a step-by-step characterization of each thin film as it is taken from the as-prepared state through the various electrochemical tests. It is argued that the nature and surface chemical composition of the different materials is crucial to determining their performance and stability.

New insight is provided in part because the samples prepared by magnetron sputtering are not necessarily equilibrium structures. An important message is that bulk composition, as determined by EDX, may not be a prime determinant of electrochemical behavior, a property that is especially dependent on surface composition. An illustration is provided by comparing the surfaces of the two thin films designated as TF1 and TF3. The latter sample had twice as much Se in the bulk as the former, but the as-prepared surfaces of both were dominated by Co, and that gave rise to similarities in initial electrochemical performance (CV analysis).

In general, the surface chemistry of all samples changed significantly as a result of electrochemical testing. It was found that any surface Co not bonded to Se dissolved in the acid environment, leaving a chalcogen-rich active surface. Accordingly, the electrochemical CV treatment can be seen as a pretreatment step, to leach out soluble components, before the actual ORR measurements are made using RDE.

This work showed that systems based on Co–Se materials are catalytically active for ORR. The active surfaces have high chalcogen-to-metal ratios and the Tafel slopes are close to -130 mV dec^{-1} , measured in the potential range 0.5–0.7 V vs RHE. The TF2 model catalyst showed the least change in surface composition during electrochemistry. Thus far, no attempt has been made to optimize the exchange current density from the thin films, an exercise that would require increasing the density of active sites. At this time, we only have some initial clues as to their nature. For example, the thin films have a nanocrystalline component based on a Co-deficient form of CoSe, and it is possible that these structures, surrounded with some extra chalcogen, may contribute to the active site for ORR. Also, it is noted that surface analysis of the thin films after electrochemical tests indicated that in the H_2SO_4 electrolyte, some Se-to-S exchange occurs, but at this time, we do not know whether or how this affects the catalytic activity.

The catalytic response and nature of the thin films were subsequently compared to a Co–Se catalyst prepared on a dispersed carbon support. It was concluded that this Co–Se catalyst has a similar active phase, OCP, and Tafel region as the model catalysts prepared as thin films. The powder catalyst appears to have a significant activity, although a direct comparison with a commercial Pt catalyst is obscured by the unknown active surface area. The methodology described of using the thin-film approach appears particularly useful for developing a better fundamental understanding of ORR on non-Pt surfaces and, in turn, for guiding the discovery and optimization of new catalysts.

Acknowledgment. We are grateful for the support of this research provided jointly by Ballard Power Systems and the United States Department of Energy under contract number DE-FC36-03GO13107. We also acknowledge support to M.T. by the Natural Sciences and Engineering Research Council of Canada. We thank Dr. K. C. Wong and Ms. M. Mager for their help.

References and Notes

- (1) Gasteiger, H. A.; Kocha, S. S.; Sompolli, B.; Wagner, F. T. *Appl. Catal., B* **2005**, *56*, 9–35.
- (2) Kordesch, K.; Simader, G. *Fuel Cells and Their Applications*; VCH Publishers: New York, 1996; pp 1–90.
- (3) Antolini, E. *J. Appl. Electrochem.* **2004**, *34*, 563–567.
- (4) Mukerjee, S.; Srinivasan, S. *J. Electroanal. Chem.* **1993**, *357*, 201–224.
- (5) Mukerjee, S.; Srinivasan, S.; Soriaga, M. P.; McBreen, J. *J. Electrochem. Soc.* **1995**, *142*, 1409–1422.
- (6) Markovic, N. M.; Radmilovic, V.; Ross, P. N., Jr. In *Catalysis and Electrocatalysis at Nanoparticle Surfaces*; Wieckowski, A., Savinova, E. R., Vayenas, C. G., Eds.; Marcel Dekker: New York, 2003; pp 311–330.
- (7) Markovic, N. M.; Schmidt, T. J.; Stamenkovic, V.; Ross, P. N. *Fuel Cells* **2001**, *1*, 105–116.
- (8) Watanabe, M.; In *Catalysis and Electrocatalysis at Nanoparticle Surfaces*; Wieckowski, A., Savinova, E. R., Vayenas, C. G., Eds.; Marcel Dekker: New York, 2003; pp 827–842.
- (9) Gattrell, M.; MacDougall, B. In *Handbook of Fuel Cells, Fundamentals, Technology and Applications*; Vielstich, W., Lamm, A., Gasteiger, H. A., Eds.; John Wiley and Sons: New York, 2003; Vol. 2, pp 443–464.
- (10) Adzic, R.; In *Electrocatalysis*; Lipkowsky, J., Ross, P. N., Eds.; John Wiley and Sons: New York, 1998; pp 197–242.
- (11) Kinoshita, K. *Electrochemical Oxygen Technology*; John Wiley and Sons: New York, 1992; pp 19–65.
- (12) Isaacs, M.; Aguirre, M.; Toro-Labbe, A.; Costamagna, J.; Paez, M.; Zagal, J. *Electrochim. Acta* **1998**, *43*, 1821–1827.
- (13) Claude, E.; Adduo, T.; Latour, J.; Aldebert, P. *J. Appl. Electrochem.* **1997**, *28*, 57–64.
- (14) Zagal, H. J.; Cárdenas-Jirón, G. I. *J. Electroanal. Chem.* **2000**, *489*, 96–100.
- (15) Faubert, G.; Lalande, G.; Côté, R.; Guay, D.; Dodelet, J.; Weng, L.; Bertrand, P.; Denes, G. *Electrochimica Acta* **1996**, *41*, 1689–1701.

- (16) Bogdanoff, P.; Herrmann, I.; Hilgendorf, M.; Dorbandt, I.; Fiechter, S.; Tributsch, H.; *J. New Mater. Electrochem. Sys.* **2004**, *7*, 85–92.
- (17) Schulenburg, H.; Stankov, S.; Schuenemann, V.; Radnik, J.; Dorbandt, I.; Fiechter, S.; Bogdanoff, P.; Tributsch, H. *J. Phys. Chem. B* **2003**, *107*, 9034–9041.
- (18) Zagal, J. H. In *Handbook of Fuel Cells, Fundamentals, Technology and Applications*; Vielstich, W., Lamm, A., Gasteiger, H. A., Eds.; John Wiley and Sons: New York, 2003; Vol. 2, pp 544–554.
- (19) Lalande, G.; Côté, R.; Guay, D.; Dodelet, J. P.; Weng, L. T.; Bertrand, P. *Electrochim. Acta* **1997**, *42*, 1379–1388.
- (20) Côté, R.; Lalande, G.; Faubert, G.; Guay, D.; Dodelet, J. P.; Dénès, G. *J. Electrochem. Soc.* **1998**, *145*, 2411–2418.
- (21) Alonso-Vante, N.; Tributsch, H. *Nature* **1986**, *323*, 431–432.
- (22) Alonso-Vante, N.; Jaegermann, W.; Tributsch, H.; Konle, W.; Yvon, K. *J. Am. Chem. Soc.* **1987**, *109*, 3251–3257.
- (23) Alonso-Vante, N.; Tributsch, H.; Solorza-Feria, O. *Electrochim. Acta* **1995**, *40*, 567–576.
- (24) Alonso-Vante, N.; Bogdanoff, P.; Tributsch, H. *J. Catal.* **2000**, *190*, 240–246.
- (25) Romero, T.; Solorza, O.; Riviera, R.; Sebastian, P. J. *J. New Mater. Electrochem. Sys.* **1999**, *2*, 111–114.
- (26) Rodriguez, F. J.; Sebastian, P. J. *J. New Mater. Electrochem. Sys.* **1999**, *2*, 107–110.
- (27) Tributsch, H.; Bron, M.; Hilgendorff, M.; Schulenburg, H.; Dorbandt, I.; Eyert, V.; Bogdanoff, P.; Fiechter, S. *J. Appl. Electrochem.* **2001**, *31*, 739–748.
- (28) Alonso-Vante, N. In *Handbook of Fuel Cells, Fundamentals, Technology and Applications*; Vielstich, W., Lamm, A., Gasteiger, H. A., Eds.; John Wiley and Sons: New York, 2003; Vol. 2, pp 535–543.
- (29) Jusys, Z.; Kaiser, J.; Behm, R. J. *Phys. Chem. Chem. Phys.* **2001**, *3*, 4650–4660.
- (30) Jusys, Z.; Schmidt, T. J.; Dubau, L.; Lasch, K.; Jörissen, L.; Garche, J.; Behm, R. J. *J. Power Sources* **2002**, *105*, 297–304.
- (31) Maillard, F.; Savinova, E. R.; Simonov, P. A.; Zaikovskii, V. I.; Stimming, U. *J. Phys. Chem. B* **2004**, *108*, 17893–17904.
- (32) Behret, H.; Binder, H.; Sandstede, G. *Electrochim. Acta* **1975**, *20*, 111–117.
- (33) Deng, C. Z.; Dignam, M. J. *J. Electrochem. Soc.* **1998**, *145*, 3507–3512; Deng, C. Z.; Dignam, M. J. *J. Electrochem. Soc.* **1998**, *145*, 3513–3520.
- (34) Williams, D. B. *Practical Analytical Electron Microscopy in Materials Science*; Electron Optics Publishing Group: Deerfield Beach, FL, 1984; pp 67–82.
- (35) Seah, M. P. In *Practical Surface Analysis*; Briggs, D., Seah, M. P., Eds.; John Wiley and Sons: New York, 1990; Vol. 1, pp 201–257.
- (36) Clavilier, J.; Faure, R.; Guinet, G.; Durand, R. *J. Electroanal. Chem.* **1980**, *107*, 205–209.
- (37) Stamenkovic, V.; Markovic, N. M.; Ross, P. J. *J. Electroanal. Chem.* **2001**, *500*, 44–51.
- (38) Bronikowski, T.; Pasiuk-Bronikowska, W.; Ulejczyk, M.; Nowakowski, R. *J. Atmos. Chem.* **2000**, *35*, 19–31.
- (39) Zhdanov, S. I. In *Selenium*, Encyclopedia of Electrochemistry of Elements; Bard, A. J., Ed.; Marcel Dekker Inc.: New York and Basel, 1975; Vol. IV–7, pp 361–392.
- (40) Streltsov, E. A.; Poznyak, S. K.; Osipovich, N. P. *J. Electroanal. Chem.* **2002**, *518*, 103–104.
- (41) Moulder, J. F.; Stickle, W. F.; Sobol, P. E.; Bomben, K. D. In *Handbook of X-ray Photoelectron Spectroscopy*; Chastain, J., King, R. C., Jr., Eds.; Physical Electronics Inc.: Eden Prairie, MN, 1995; pp 96–97.
- (42) Van der Heide, H.; Hemmel, R.; Van Brugger, C. F.; Haas, C. *J. Solid State Chem.* **1980**, *33*, 17–25.
- (43) Mandale, A. B.; Badrinarayanan, S.; Date, S. K.; Sinha, A. P. B. *J. Electron Spectrosc. Relat. Phenom.* **1984**, *33*, 61–72.
- (44) *Binary Alloy Phase Diagrams*, 2nd ed.; Massalski, T. B., Okamoto, H., Subramanian, P. R., Kacprzak, L., Eds.; ASM International: Materials Park, OH, 1990; Vol. 2, pp 1235–1237.
- (45) Cullity, B. D. *Elements of X-ray Diffraction*; Addison-Wesley Pub. Co.: Boston, MA, 1978; pp 92–188.
- (46) Zhan, J.; Yang, X.; Li, S.; Xie, Y.; Yu, W.; Qian, Y. *J. Solid State Chem.* **2000**, *152*, 537–539.
- (47) García-García, F. J.; Larsson, A. K.; Norèn, L.; Withers, R. L. *Solid State Sci.* **2004**, *6*, 725–733.
- (48) Sirk, A. H. C. Ph.D. Thesis, University of Calgary, Calgary, Alberta, Canada, 2004.
- (49) Faubert, G.; Côté, R.; Guay, D.; Dodelet, J. P.; Dénès, G.; Poleunis, C.; Bertrand, P. *Electrochim. Acta* **1998**, *43*, 1969–1984.